High-temperature strengthening mechanisms of Laves and B2 precipitates in a novel ferritic alloy

Tianyi Chen, Chad M. Parish, Ying Yang, Lizhen Tan

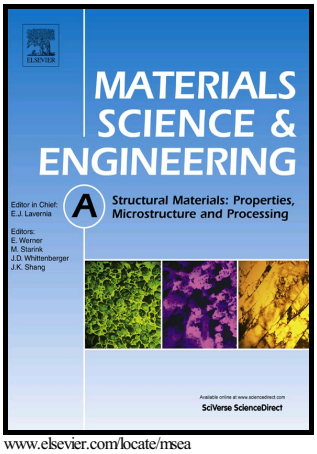

www.elsevier.com/locate/msea

PII: S0921-5093(18)30197-7
DOI: https://doi.org/10.1016/j.msea.2018.02.013
Reference: MSA36100

To appear in: *Materials Science & Engineering A*

Received date: 23 December 2017
Revised date: 1 February 2018
Accepted date: 4 February 2018

Cite this article as: Tianyi Chen, Chad M. Parish, Ying Yang and Lizhen Tan, High-temperature strengthening mechanisms of Laves and B2 precipitates in a novel ferritic alloy, *Materials Science & Engineering A*, https://doi.org/10.1016/j.msea.2018.02.013

High-temperature strengthening mechanisms of Laves and B2 precipitates in a novel ferritic alloy[†]

Tianyi Chen*, Chad M. Parish, Ying Yang, Lizhen Tan*
Oak Ridge National Laboratory, Oak Ridge, TN 37831, USA

Corresponding authors:
Tianyi Chen: tianyichn@gmail.com
Lizhen Tan: tanl@ornl.gov

Abstract:
Laves and B2 phases were engineered in a newly-designed advanced ferritic alloy. Under creep test at 650ºC with 120 MPa, the material showed a steady-state minimum creep rate of 1×10^{-4} h^{-1}, about one order of magnitude lower than T91. Microstructural characterization of the ferritic alloy revealed primarily ductile with partial brittle fractures after the creep test. Coarse Laves phase (~1 μm) was observed associating with the partial brittle fracture, resulting in reduced creep ductility. However, fine Laves phase (~100 nm) helped dimple ductile fracture, strengthening the material through impeding the motion of dislocations and boundaries. Unlike the B2 precipitates remained coherent with the classic Orowan bypassing mechanism at the brittle location, some of the B2 precipitates at the ductile location became incoherent and have a dislocation pinning effect. The change into incoherent B2 precipitates, together with the nucleation of ultrafine (~40 nm) Laves phase precipitated during the creep test, would compensate for the coarsening-induced loss of Orowan strengthening of coherent B2 precipitates.

Key words: creep; fracture; microstructure; dislocation; Orowan strengthening.

I. Introduction

Ferritic martensitic (F/M) alloys are candidate nuclear materials because of their superior swelling resistance and structural stability under irradiation, lower thermal expansion, and higher thermal conductivity compared with the widely used austenitic steels [1, 2]. However, F/M alloys generally suffer significant recovery of dislocations and subgrains at temperatures above ~600°C and ferrite-to-austenite phase transformation at temperatures above ~800°C. On the other hand, ferritic alloys, without interstitial austenite stabilizers such as C and N, do not suffer the phase transformation. To compensate for the reduced strength by the decreased dislocation density and vanished lath boundaries in F/M alloys [1], ferritic alloys usually exploit precipitate strengthening, in addition to solid solution and grain boundary strengthening.

In alloy systems, the change in solid solubility with temperature makes it possible to introduce precipitation in the material through heat treatment. The types and volume fractions of the precipitates can be controlled through adjusting the alloy compositions and aging temperatures, based on the thermodynamics [3]. The precipitates can impede the motion of dislocations and thus increase the materials' strength. Precipitation strengthening has been employed in a variety of ferritic alloys [3-12], with intermetallics, carbides and nitrides being the most common precipitates. Table 1 lists some representative studies, in which different kinds of precipitates strengthened the materials with varied mechanisms. The operating strengthening mechanisms of the precipitates seem to correlate with the precipitate size and the level of coherency with matrix. It has been shown that coherent B2 precipitates below 3 nm in diameter, with minimal lattice misfit, can strengthen through the back-stresses caused by the chemical ordering effect at room temperature [6], while coherent B2 precipitates having a diameter larger than 10 nm can impede the dislocation motion through Orowan bypass mechanism [5]. The dislocation-precipitate detachment mechanism operates when the precipitates begin to lose coherency as a result of coarsening, usually as a result of thermal annealing, and likely be accelerated with stress [5, 12, 13]. Carbides that are coherent with the matrix can also significantly increase the strength of the materials, with the strengthening effect well-predicted by the Ashby-Orowan mechanism [11]. On the other hand, incoherent precipitates such as Laves phase exert strengthening by pinning dislocations and boundaries [8, 10]. The size and volume fraction of the incoherent precipitates were observed to be critical to the strengthening effect [10].

Table 1. Literature reporting precipitation strengthening of different ferritic alloys.

Precipitation phase	Strengthening mechanisms.	Ref.
Coherent B2 NiAl	Orowan bypass and detachment mechanisms.	[5]
Coherent B2 Ni(Al,Fe)	Backstress induced by chemical ordering effect due to minimal lattice misfit and ultra-small precipitate size (< 3 nm).	[6]
Coherent Fe_3Zr	Dislocation-particle interaction.	[7]
Laves	Dislocation and boundary pinning.	[8]
Carbide	Ashby-Orowan mechanism.	[11]

A series of advanced ferritic alloys were designed and fabricated with the aid of computational thermodynamics to incorporate both coherent B2 and incoherent Laves phase for precipitation strengthening. The two types of precipitates were expected to have distinct sizes to achieve a

combinatorial strengthening effect of the new alloys, which was demonstrated in this study by direct observations of the precipitate-dislocation interactions using transmission electron microscopy (TEM). Some evidence of precipitate coarsening accelerated by stress at high temperature was presented. The effects of precipitate type and size on the ductility and strength of the material was discussed. The outcome of this study would shed light on designing advanced alloys with balanced phase constitution for superior performance.

II. Material and Method

A ferritic alloy with a nominal composition of Fe–12Cr–3W–3Ni–3Al–1Zr in weight percentage (wt%) was designed to contain precipitates of Laves and B2 phases in fully ferritic matrix at temperatures up to its melting point. An experimental ingot, about 700 g, of the alloy with the target composition (purity >99.95 wt%) was fabricated using arc-melting and drop casting in a titanium-gettered argon atmosphere. The ingot was annealed at 1100°C for 15 min in an argon atmosphere and rolled to ~6.3 mm from initial ~25.4 mm at 1000°C, followed by air cooling to room temperature. The rolled piece was aged at 800°C for 5h and then 650°C for 5 h, to favor Laves and B2 phases precipitation.

Creep testing was conducted in accordance with the American Society for Testing and Materials (ASTM) standard E139-11, *Standard Test Methods for Conducting Creep, Creep-Rupture, and Stress-Rupture Tests of Metallic Materials* [14]. The testing was conducted at 650°C and 120 MPa using type SS-3 miniature specimens with a gauge section of 7.62 × 1.52 × 0.76 mm, which were extracted from the material with the gauge length parallel to the rolling direction.

Scanning electron microscopy (SEM: JEOL 6500F), TEM (JOEL 2100F), and scanning transmission electron microscopy (STEM: Thermo Talos F200X [15]) were used to characterize the samples in the as-received and creep-ruptured conditions. Particularly, energy-filtered TEM technique was used to produce sample thickness mapping for the estimation of precipitate volume fractions; SEM backscattered electron (BSE) and STEM high-angle annular dark-field (HAADF) imaging techniques were employed to have Z-contrast for phase suggestion with higher atomic number on average for brighter phases. The precipitate types were further confirmed with the combination of energy dispersive X-ray spectroscopy (EDS) and selected-area electron diffraction (SAED). SEM observations were conducted on the fracture surfaces of the creep-ruptured sample and a bulk sample in the as-received condition. The as-received sample was prepared to a mirror-finish following conventional metallographic sample grinding and polishing. For TEM based characterizations, electron-transparent lamellae were prepared from the creep-ruptured and bulk samples using focused-ion-beam (FIB: FEI Versa 3D) techniques. Before surface trenching, a layer of Pt was deposited using 5 keV electron beam to protect the fracture surface. Trenching and initial thinning was conducted with 30 keV Ga^+ ion. The Ga^+ ion energy was gradually reduced to 2 keV for final polishing to reduce the ion-induced damages.

III. Results

The microstructures of the material in the as-received condition are shown in Fig. 1 obtained using SEM-BSE (a and b) and STEM-HAADF (c-e) techniques. The SEM-BSE image in Fig. 1a

shows grains in two different sizes, with fine grains (~10 μm) on the right-hand side and coarse grains (~40 μm) on the left-hand side. The variation in the grain sizes was attributable to the incomplete recrystallization during hot rolling, primarily resulting from the local pinning effects of the precipitates [16], e.g., the particles in light gray in Fig. 1a distributed along the prior austenite grain or subgrain boundaries. The light gray particles are Laves phase (primarily Fe_2Zr) according to EDS analysis and the nature of BSE images, because of their higher atomic number. The Laves phase precipitates were also shown in the HAADF images in Fig. 1c and d at the grain boundaries. The bright particles (suggesting high-Z) and the SAED inset of Fig. 1c for the arrowed particle at the $[11\bar{2}0]$ zone axis confirm the C14 Laves structure of the particles. The size for the Laves phase ranges from ~50 nm to ~10 μm from the TEM and SEM characterizations. Most of the Laves phase precipitates were found decorating grain boundaries, although some were found to be intragranular. Other than the bright Laves phase, the dark precipitates of ~10 nm in diameter are observed in Fig. 1b and e at higher magnifications. These precipitates were found to be Ni and Al rich using STEM-EDS and their crystal structure was confirmed to be B2-type NiAl. The SAED pattern in the inset of Fig. 1e shows strong and weak (pointed by an arrow) diffracted spots corresponding to the [001] zone axis of the ferritic matrix and the NiAl precipitates, respectively, indicating their cubic-on-cubic coherency relationship. The density of the NiAl precipitates is ~2×10^{22} m^{-3} with the mean precipitate diameter measured to be 11 ± 2 nm, yielding a volume fraction of ~1.5 % assuming spherical shape for precipitates.

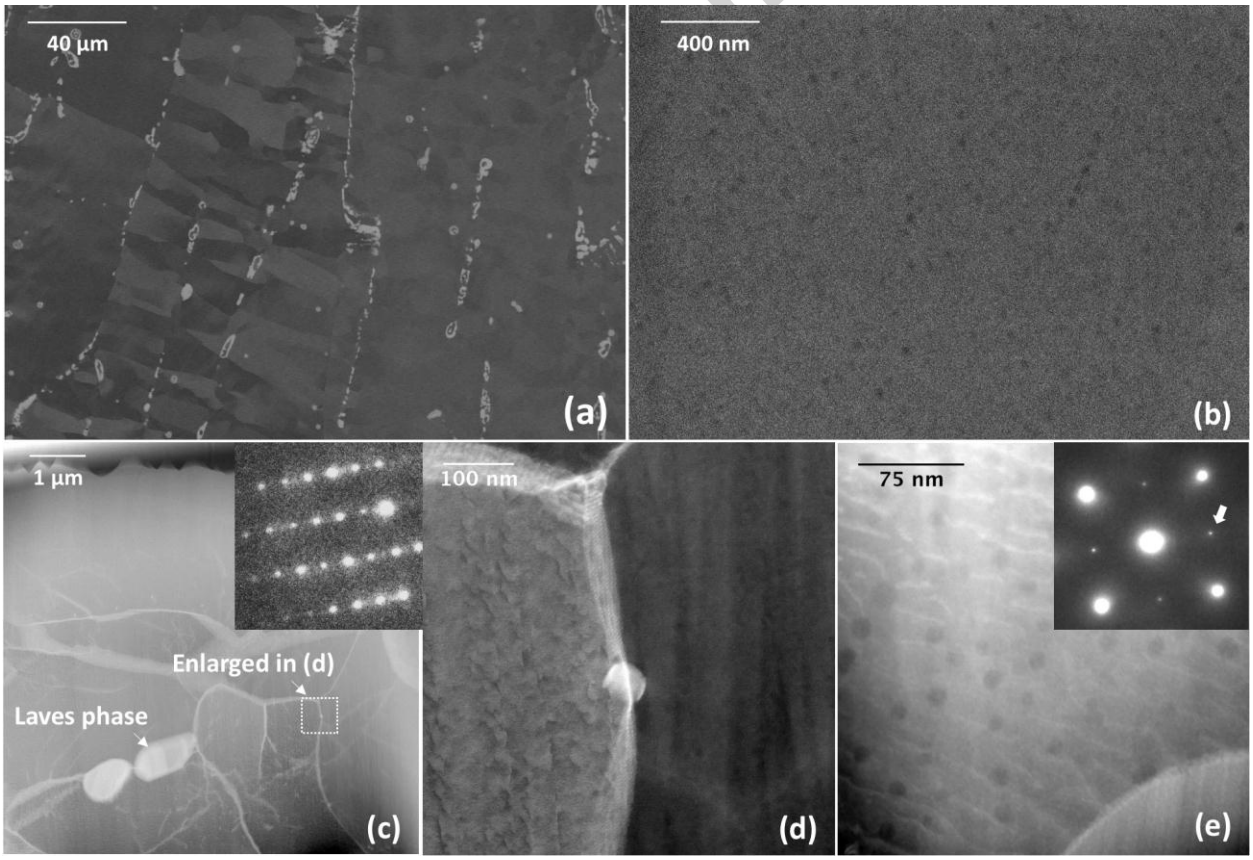

Figure 1. SEM-BSE micrographs of the as-received samples at two magnifications showing (a) grain structure with coarse Laves phase precipitates and (b) B2-type NiAl precipitates. STEM-

HAADF micrographs with SAED pattern insets illustrating the morphologies and crystal structures of the (c, d) Laves phase precipitates and (e) B2-type precipitates; (d) is enlarged from the labeled square in (c).

Fig. 2 shows the strain-time curve of the creep test at 650 ºC with 120 MPa load. The typical three-stage curve shows a relatively short primary stage. The steady-state secondary stage, taking place in between about 3-60 hours, has a minimum strain rate of ~1×10^{-4} h^{-1}. The minimum creep rate is about one order of magnitude lower than that of T91 steel at a similar condition [17]. After ~60 hours, the strain rate began to deviate from the minimum creep rate in an accelerated manner, which indicates the beginning of the tertiary stage according to ASTM E139-11.

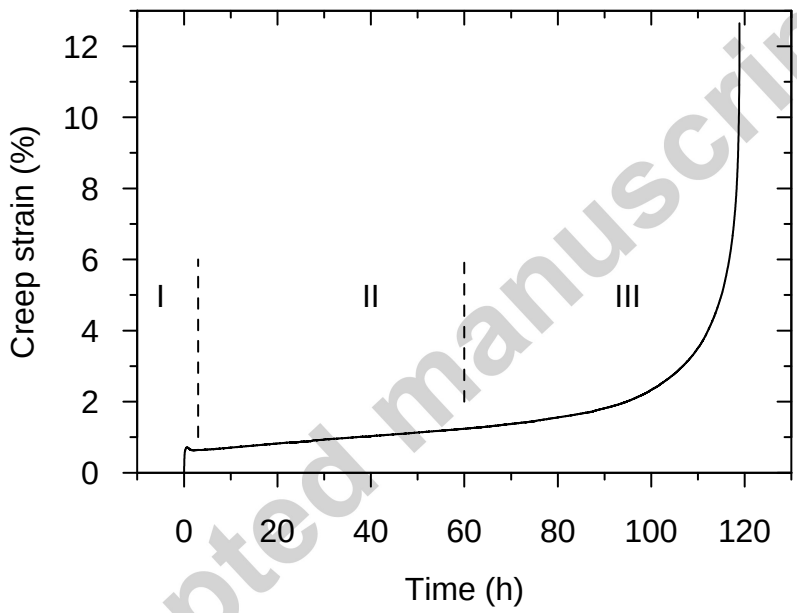

Figure 2. Creep strain-time curve for the test at 650ºC and 120 MPa.

The fractography of the creep-ruptured sample primarily exhibited dimple ductile with partial cleavage brittle features as shown in Fig. 3a. The fracture surface is outlined with a dotted line. Fig. 3b shows a higher magnification image of the ductile fracture from the center of the sample where the necking led to the most area reduction in Fig. 3a. Most of the dimples contain a particle at the core, some of which were pointed by the white arrows in Fig. 3b. Composition analysis using EDS shows that the core particles are Zr-rich, and thus believed to be Laves phase precipitates. The Laves phase precipitates observed in the ductile locations are generally less than 4 μm in diameter. As will be shown later, the sizes were overestimated because of the oxidation of the particles. The dimples were formed as a result of creep void nucleation at the cores, and subsequent void growth and coalescence under stress.

Similarly, a higher magnification image of the brittle fracture is shown in Fig. 3c. Both intragranular fracture and intergranular decohesion were noticed with the former being the dominant. Some river marks and spherical features were observed on the surfaces of

intragranular fractures, which were respectively marked by black and white arrows in Fig. 3c. The fracture was initialized with multiple cracks growing simultaneously. When two cracks joined together, through shear or secondary cleavage, a cleavage step formed. The junction of cleavage steps resulted in the river marking features [18]. The spherical features are typically around 3 - 20 μm in diameter, which were later confirmed to be Laves phase precipitates by TEM. The precipitates found in the brittle fracture sites were in general larger than those presented in the ductile fractures.

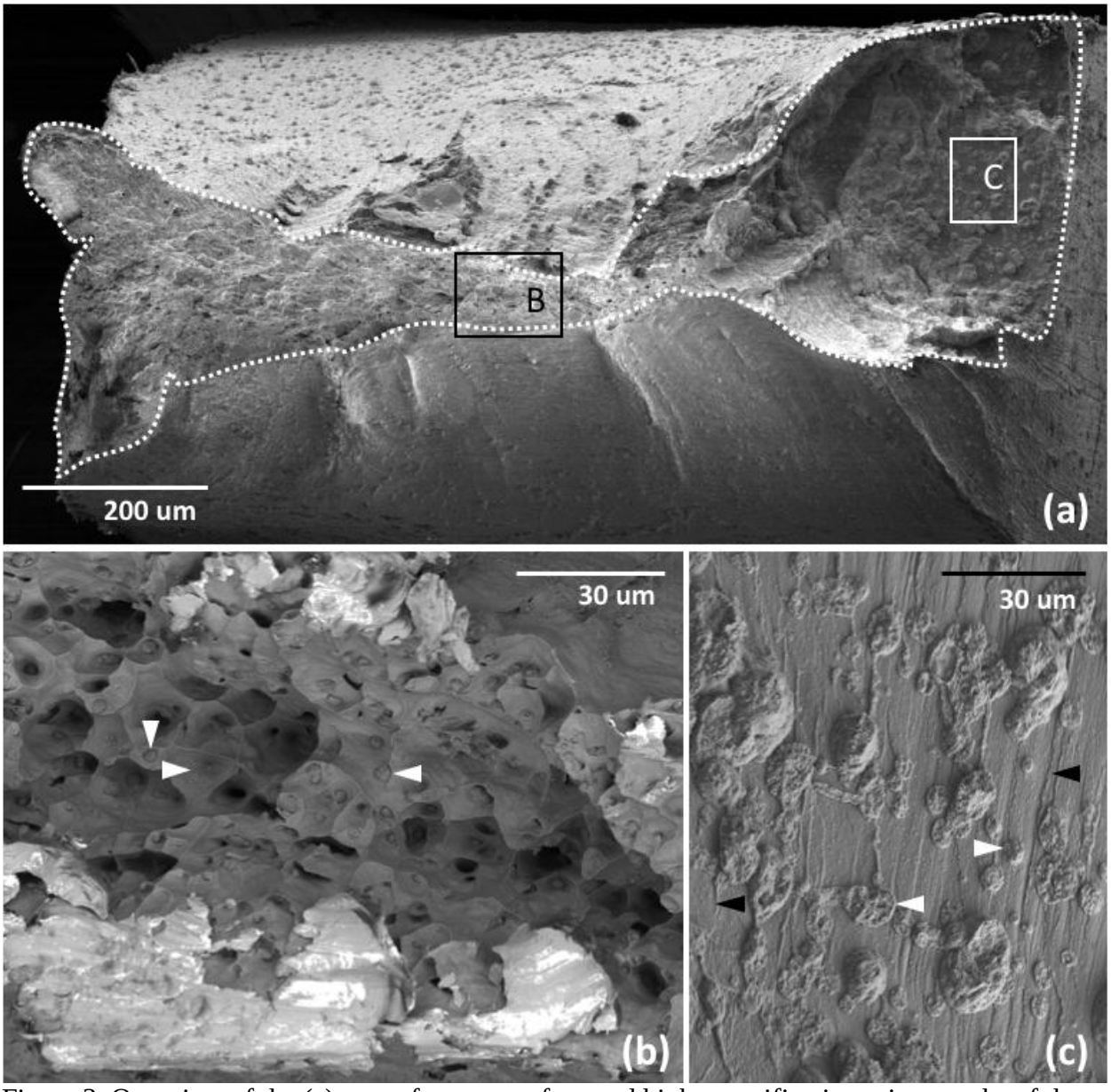

Figure 3. Overview of the (a) creep fracture surface and high magnification micrographs of the (b) ductile and (c) brittle regions. The black boxes in (a) marked as B and C indicate the regions of (b) and (c), respectively. White arrows indicate the Laves phase precipitates, and the black arrows indicate the river marks.

The FIB lift-out samples from the ductile and brittle fracture surfaces are shown in Fig. 4a and b, respectively. Before the samples were lifted-out, a protective Pt layer was deposited on the fracture surfaces schematically marked with the dotted lines in Fig. 4a and b. The ductile surface shows curvatures from the dimples, while the brittle surface has segments connected with steps manifested as the river marks in Fig. 3c. As suggested by the creep curve in Fig. 2, the material underwent significant deformation in the tertiary creep stage. High densities of dislocation network walls were observed in response to the high strain at the necking area, shown as the cell structures in Fig. 4a. In contrast, the dislocation density is much lower underneath the brittle surfaces, indicating that the brittle fracture happened without undergoing the tertiary stage of creep.

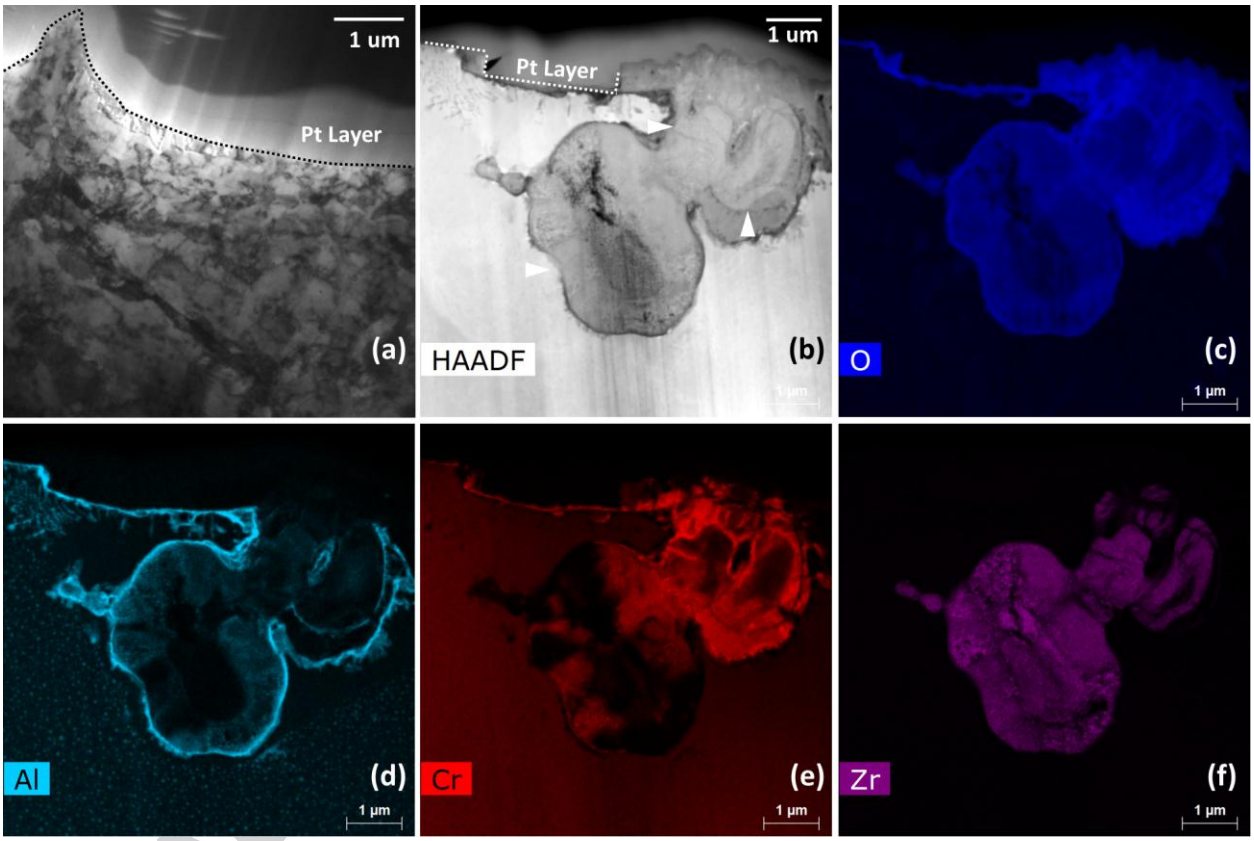

Figure 4. STEM micrographs showing the regions near the (a) ductile (bright-field) and (b) brittle (HAADF) fracture surfaces. (c-f) compositional maps of the brittle sample. The maps were smoothed with a 3×3 pixel smoothing kernel.

The coarse particles in Fig. 4b, pointed by white triangles, were identified to be Laves phase particles that oxidized during the creep test. The chemical analysis using EDS, as shown in Fig. 4 c-f, revealed that the oxide forms within the whole particles, with an Al-rich layer at the particle-matrix interface. Chromium and zirconium segregated within the oxide. Chromium tend to enrich near the outer shell, while zirconium is slighted enriched near the core.

Fig. 5 presents compositional mapping, accompanied with the respective HAADF images, of the cross-sectional samples underneath the ductile fracture in Fig. 5a-f and the brittle fracture in Fig. 5g-l. The micrographs were taken ~4-6 µm in depth from the fracture surfaces. The Fe-maps are

not included as they are approximately identical to the Cr-maps. The Ni and Al maps in Fig. 5 shows the densities of the B2 precipitates (NiAl) to be 2.3 ± 0.5 and 1.9 ± 0.6 ($\times 10^{20}$ m^{-3}) for the brittle and ductile locations, respectively, which are two orders of magnitudes lower compared with the as-received NiAl density of ~2×10^{22} m^{-3}. Although visually higher density appears for the brittle location because of its greater TEM sample thickness (100 ± 20 nm of Fig. 5a vs. 230 ± 70 nm of Fig. 5g), the densities of B2 precipitate in the brittle and ductile locations are roughly the same within the statistical errors. Primarily driven by thermal aging, the B2 precipitates coarsened to a mean diameter of 50 ± 10 nm in the brittle location. In contrast, at the ductile location, the B2 precipitates elongated along the tensile direction, with the mean major and minor axis being 70 ± 20 and 50 ± 10 nm, respectively. Some of the coarsened particles lost coherency to the matrix.

Fig. 5d shows several Zr-rich ultrafine precipitates of < 40 nm in diameter in the ductile sample. SAED-based crystal structure identification was not conducted because of the small sized and low densities of these precipitates; however, the chemical compositions of the Zr-rich fine precipitates suggest that they could be the Laves phase. The density of the Zr-rich ultrafine precipitates in the ductile-fractured sample was measured to be 1×10^{19} m^{-3}, which was not observed in the as-received or brittle-fractured conditions, suggesting that the Zr-rich ultrafine precipitates nucleated during the ductile creep deformation.

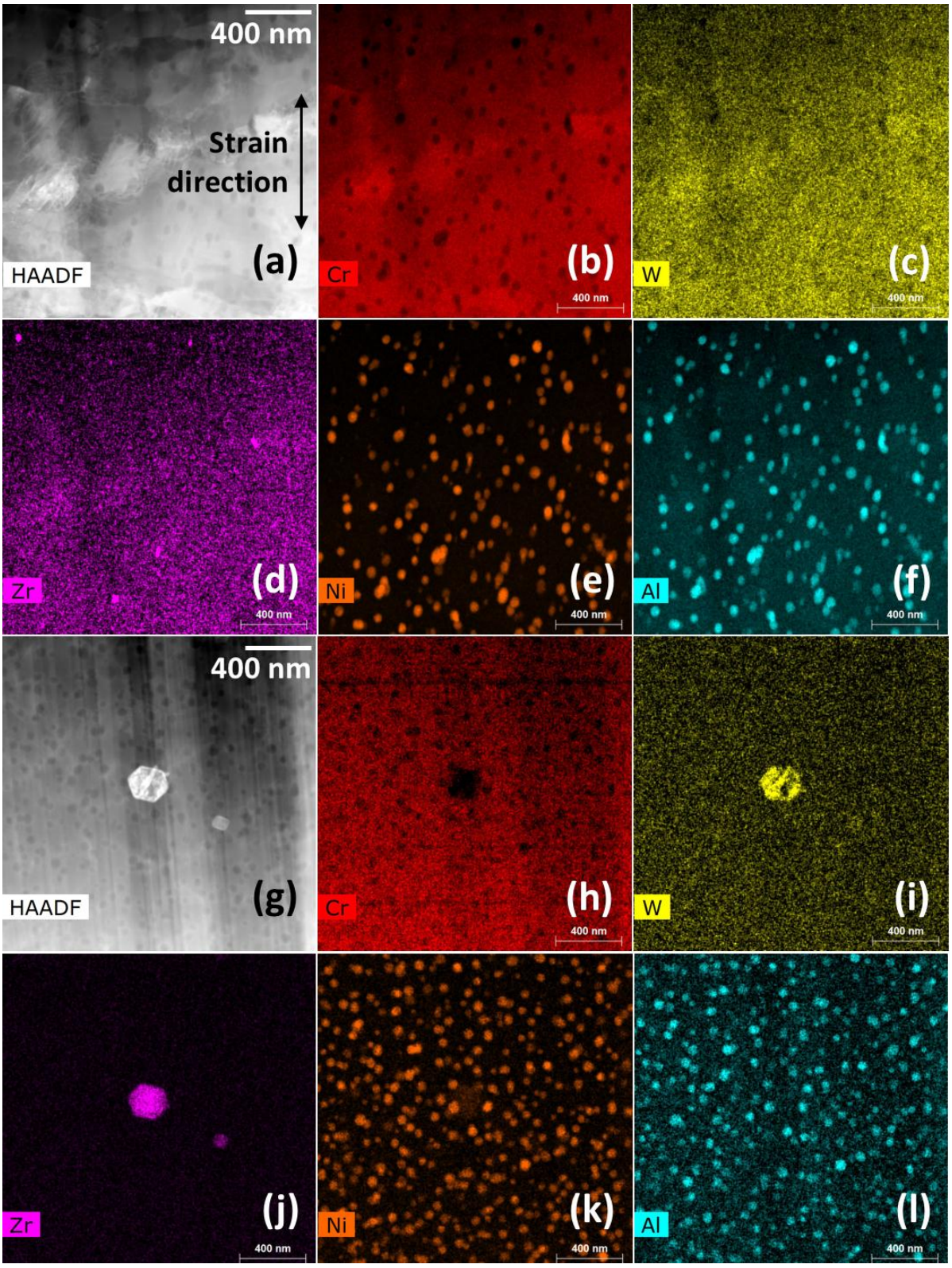

Figure 5. HAADF images and compositional maps of the samples near the ductile fracture in (a-f) and the brittle fracture in (g-l). The applied stress direction is vertical in the images. The maps were smoothed with a 3×3 pixel smoothing kernel.

Fig. 6 shows bright-field STEM micrographs beneath the ductile fracture surface (a-c) and the brittle fracture surface (d-e). Subgrains with diameters less than 500 nm formed at the ductile location as shown in Fig. 6a. Dislocations of significantly high density were observed in some of the grains, indicating high level of local deformation. Bright-field STEM in higher magnifications in Fig. 6b-c show the coarsened B2 precipitates having different diffraction contrast from the matrix. This is different from the scenario shown in Fig. 6d-e, where diffraction contrast between the B2 precipitates (e.g., pointed by white triangles) and the matrix was dim due to their cubic-on-cubic coherency relationship. The comparison between Fig. 6b-c and Fig. 6d-e indicates that the B2 precipitates lost their coherency with the matrix under the extremely high strain near at ductile location. With the loss of coherence, precipitates can develop an attractive interaction with dislocations, impeding dislocation and boundary motions [5], consequently favoring subgrain formation constituted by the dislocation wall structures as shown in Fig. 6b.

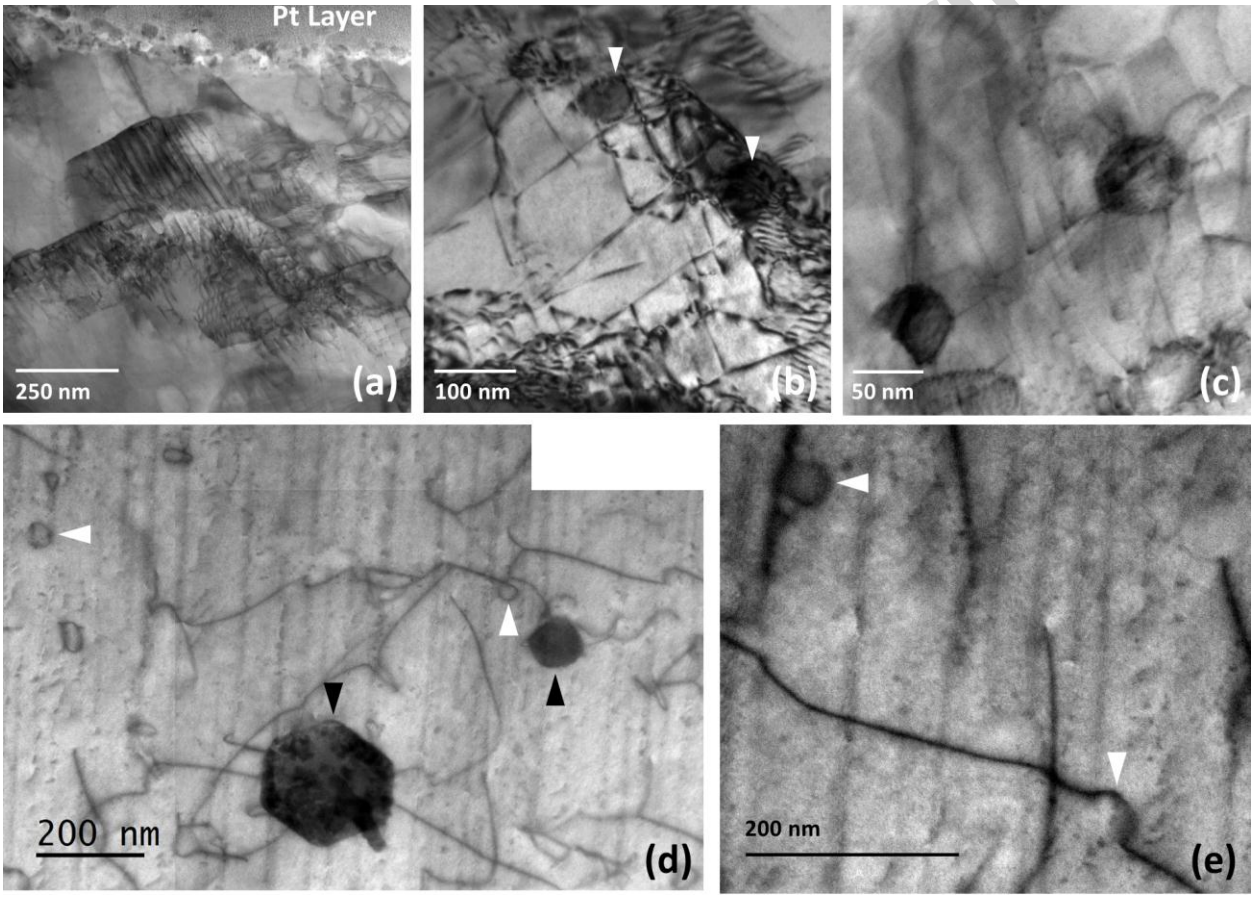

Figure 6. STEM bright-field micrographs: near the ductile fracture surface showing (a) dislocation slip traces and (b-c) coarsened B2 precipitates pinning subgrain boundaries and dislocations; (d-e) near the brittle fracture surface showing the interactions between dislocations and B2/Laves phases.

Dislocation-precipitate interactions were also observed beneath the brittle fracture surface, where the local strain was low because the fracture took place before the tertiary creep stage. Some B2

precipitates were observed to be surrounded by dislocation loops (Fig. 6d), indicating dislocations bypassing around precipitates through Orowan bowing (Fig. 6e). Some Laves phase precipitates with diameters of ~100 nm (black arrows in Fig. 6d) were also observed in the sample. They can interact with dislocations through the pinning effect [8, 10]. The particle-matrix interface might also serve as source of dislocations with the accumulation of local stress.

V. Discussion

Table 2 summaries the characterized features in the current study, separating the ductile and the brittle behavior of the creep sample. The most significant difference between the ductile and brittle facture of the sample is the pre-existing inhomogeneous distribution of the Laves phase precipitates. Measured from the fracture surfaces shown in Fig. 3, the Laves precipitates are significantly larger in the brittle site than the ductile site. Although oxidation of the precipitates caused overestimation of the precipitate sizes for both sites, it can be concluded that the brittleness is associated with the populated coarse precipitates of the Laves phase.

Table 2. Laves and B2 precipitates characterized at the ductile and brittle fracture locations of the creep tested sample.

Precipitates		Fracture type (Area reduction [1])	
		Ductile (~ 80 %)	Brittle (~ 30 %)
Laves phase	Mean diameter (μm) at the fracture surface under SEM [2]	1.7 ± 0.8	6 ± 5
	Mean diameter (nm) beneath the fracture surface.	≤ 40 (Zr-rich precipitates nucleated during the creep test), in addition to ~100 (pre-existing, as seen in the as-received condition)	~50 to ~1000 (pre-existing, with size, morphology and density comparable to the as-received condition)
B2 phase	Mean diameter (nm)	a = 70 ± 20; b = 50 ± 10	a = 50 ± 10
	Number density ($\times 10^{20}$ m^{-3})	1.9 ± 0.6	2.3 ± 0.5
	Volume fraction (%)	1.6 ± 0.8	1.7 ± 0.6
	Morphology	Elongated along the tensile direction	Spherical

[1] Estimated from Fig. 3a referring to the initial dimension of the sample gauge section.
[2] The fracture surface suffered oxidation, tending to cause overestimation for the precipitate sizes

The core-shell structure of the oxides of the Laves phase precipitates in Fig. 4b-f provides additional evidence of the detrimental role of the coarse precipitates. Although detailed kinetics and thermodynamics of the Laves phase oxidation are beyond the scope of this study, it is believed that the Zr-O was formed by inward diffusion of oxygen because of the higher affinity to oxygen of Zr and low diffusivity of Zr compared to other alloying elements. The surface oxide layer of the reactive element Al suggests that decohesion might have occurred at the interface of the precipitate and the matrix during the creep test, providing channels for oxygen to interact with the Laves phase from the interface. This hypothesis is supported by the observed cavities at the precipitate-matrix interfaces, implying that cracks could be initiated at the particles and then

easily propagated through the interface between the coarse Laves phase precipitate and the matrix.

The finer Laves precipitates (~100 nm) are beneficial to the creep strength of the material without increasing brittleness. As shown in Fig. 3b, the fine Laves phase does not cause brittleness as does the coarse Laves precipitates in Fig. 3c. This is because the interactions between Laves phase particles and dislocations are size sensitive [19] and dislocations could bypass and detach from finer particles more easily. At the same time, the incoherent Laves-phase particles can exert an attractive interaction to the dislocations, enabling the dislocation pinning effect as a strengthening mechanism.

In this study, the sample inhomogeneity degraded the creep life of the sample. As shown in Fig 1a, the significant variation in grain sizes resulted from the incomplete recrystallization could result in in-uniform deformation and thus local stress concentrations. On the other hand, the coarse Laves phase particles (~1 μm) probably caused the local brittle fracture as observed in Fig. 3. Because the brittle Laves phase precipitates could not accommodate the plastic strain in the ductile matrix, they might either break up or be separated from the matrix [18, 19], resulting in micro-cracks and further propagation into cracks causing intragranular and intergranular fractures. In Fig. 2, a notable creep rate increase occurred after ~60 hours, marking the end of the steady-state creep stage. The cracking from the brittle side of the sample might have expedited the end of the secondary creep stage. To optimize the material mechanical performance, the oversized Laves phase should be avoided, which requires thermodynamics-based adjustments of material composition and processing [3].

The B2 precipitates were found to be beneficial to the creep strength of the material. It has been reported that the cutting mechanism operates when the B2 precipitates were less than 3nm in diameter [6]. This mechanism was not observed in this study because the size of B2 precipitates in the as-received condition was 11 ± 2 nm and further coarsened to ~50 nm in diameters. As demonstrated in Fig. 6d and e, the Orowan bowing mechanism is active for precipitates of such sizes. As shown in Table 2, the coarsening of the B2 precipitates did not change the volume fraction of the B2 phase, because the B2 phase is thermal stable benefited from the heat treatment. With the increase in the precipitate size from ~11 nm to ~50 nm, the number densities of the B2 phase precipitates reduced by 2 orders of magnitude, which is equivalent to more than 4 times increase in the mean planar center to center distance between precipitates [20], leading to a reduction of ~70 % in Orowan dislocation bypass strengthening. This is understandable with the equation of $\Delta\sigma = \sqrt{\frac{6}{\pi}} M\alpha\mu b \frac{\sqrt{f}}{d}$ modified from Ref. [15], where $\Delta\sigma$ is the change in strength, M the Taylor factor, α the strength factor, μ the shear modulus, b the magnitude of the Burgers vector of the moving dislocation, f volume fraction and d the size (diameter) of the particles. The current case only has d and α as variables, suggesting the change in strength is primarily dependent on d with small influence from α according to Ref. [21].

The coarsening of B2 precipitates was primarily resulted from the thermal aging effect, but the straining also played a critical role. This is indicated by the larger value of the kinetics constant k obtained from the ductile site than that of the brittle site. The volume-diffusion-controlled coarsening of precipitates can be described by $\bar{r}^3 - \bar{r}_0^3 = kt$, where r is the radius of the

coarsened precipitates, r_0 the radius of the as-received precipitates, and t the time [12]. Based on the data given in Table 2, the kinetics constants for the ductile site and brittle site are 162 and 136 nm^3/h, respectively, which are comparable to the values determined by Calderon in a similar system at 700ºC [12]. The kinetics constant of coarsening is higher in the highly-deformed ductile site than that in the brittle site, because the high density of dislocations and subgrain boundaries at the ductile site served as diffusion pipes, together with a solute drag effect exerted through dislocation motion [13]. In addition, the elongated shape of the precipitates indicates that the coarsening of the B2 precipitates was facilitated along the tensile direction.

The coarsening of B2 precipitates reduced the their Orowan stress, meanwhile, made some of the precipitates lost their coherency to the matrix as their size increased. As shown in Fig. 6 b and c, the incoherent B2 precipitates pinned dislocations and cell boundaries, likely through an attractive interaction between the incoherent interface and the dislocations [5]. Given that the incoherent particles would have a greater strength factor α than the initial coherent particles [15], the coarsening-induced loss of precipitate coherency could compensate the reduced Orowan strengthening. In addition, as shown in Fig. 5d, formation of ultrafine Laves precipitates (~40 nm) occurred during creep test, which is a result of the enhanced diffusion under stress [13] and possibly enhanced nucleation with high density of dislocations. Such ultrafine precipitates of the Laves phase have also been reported to benefit the creep resistance of alloys [10].

VI. Conclusion

The analysis of the creep-ruptured sample, having primarily ductile and partial brittle fractures, provided essential understanding of the strengthening mechanisms of B2 and Laves phases. The coherent B2 precipitates exert Orowan strengthening while the fine Laves phases precipitates (~100 nm) pin dislocations and boundaries and potentially serve as a source of dislocations. However, the oversized Laves phase particles (> ~1 μm) tended to cause cracks at the particle-matrix interface, and increase brittleness. During the creep test at 650°C, coarsening of the B2 precipitates weakens Orowan strengthening. On the other hand, some coarsened B2 precipitates evolved from coherent to incoherent B2 particles under larger deformation, which could pin dislocations more strongly. Ultrafine Zr-rich Laves particles (≤ ~40 nm) were also observed to form during the creep test, which might also pin dislocations. Thermodynamics-based alloy optimization is needed to take benefit of the synergistic strengthening mechanisms of the B2 and Laves phases and avoid the embrittlement caused by the oversized Laves phase particles.

Acknowledgements

The material is based upon work supported by the U.S. Department of Energy, Office of Nuclear Energy, a Nuclear Energy Enabling Technologies FY2015 Award, under Contract No. DE-AC05-00OR22725. This research was performed, in part, using instrumentation (Talos F200X) provided by the Department of Energy, Office of Nuclear Energy, Fuel Cycle R&D Program and

the Nuclear Science User Facilities. The authors would like to thank Doctors Z. Fan and D. Zhang from ORNL for reviewing this manuscript.

Reference:

[1] L. Tan, L.L. Snead, Y. Katoh, Development of new generation reduced activation ferritic-martensitic steels for advanced fusion reactors. J. Nucl. Mater. 478 (2016) 42-49.
[2] T. Chen, E. Aydogan, J.G. Gigax, D. Chen, J. Wang, X. Wang, S. Ukai, F.A. Garner, L. Shao, Microstructural changes and void swelling of a 12Cr ODS ferritic-martensitic alloy after high-dpa self-ion irradiation. J. Nucl. Mater. 467 (2015) 42-49.
[3] T. Chen, Y. Yang, L. Tan, Phase stability in the Fe-rich Fe-Cr-Ni-Zr alloys. Metall. Mater. Trans. A, 48A (2017) 5009-5016.
[4] D.V.V. Satyanarayana, G. Malakondaiah, D.S. Sarma, Steady state creep behavior of NiAl hardened austenitic steel, Mater. Sci. Eng., A 323 (2002) 119-128.
[5] S.M. Zhu, S.C. Tjong, J.K.L. Lai, Creep behavior of A β'(NiAl) precipitation strengthened ferritic Fe-Cr-Ni-Al alloy. Acta Mater. 46 (1998) 2969-2976.
[6] S. Jiang, H. Wang, Y. Wu, X. Liu, H. Chen, M. Yao, B. Gault, D. Ponge, D. Raabe, A. Hirata, M. Chen, Y. Wang, Z. Lu, Ultrastrong steel via minimal lattice misfit and high-density nanoprecipitation. Nature 544 (2017) 460-464.
[7] D.G. Morris, M.A. Munoz-Morris, L.M. Requejo, New iron-aluminium alloy with thermally stable coherent intermetallic nanoprecipitates for enhanced high-temperature creep strength. Acta Mater. 54 (2006) 2335-2341.
[8] B. Kuhn, C. Asensio Jimenez, L. Niewolak, T. Hüttel, T. Beck, H. Hattendorf, L. Singheiser, W.J. Quadakkers, Effect of Laves phase strengthening on the mechanical properties of high Cr ferritic steels for solid oxide fuel cell interconnect application. Mater. Sci. Eng., A 528 (2011) 5888-5899.
[9] D.N. Seidman, E.A. Marquis, D.C. Dunand, Precipitation strengthening at ambient and elevated temperatures of heat-treatable Al(Sc) alloys. Acta Mater. 50 (2002) 4021-4035.
[10] Y. Yamamoto, M. Takeyama, Z.P. Lu, C.T. Liu, N.D. Evans, P.J. Maziasz, M.P. Brady, Alloying effects on creep and oxidation resistance of austenitic stainless steel alloys employing intermetallic precipitates. Intermetallics 16 (2008) 453-462.
[11] Y. Funakawa, T. Shiozaki, K. Tomita, T. Yamamoto, E. Maeda, Development of high strength hot-rolled sheet steel consisting of ferrite and nanometer-sized carbides. ISIJ International, 44 (2004), 1945-1951.
[12] H. Calderon, M.E. Fine, Coarsening kinetics of coherent NiAl-type Precipitates in Fe-Ni-Al and Fe-Ni-Al-Mo alloys, Mater. Sci. Eng., 63 (1984) 197-208.
[13] M. Hättestrand, H.-O. Andrén, Influence of strain on precipitation reactions during creep of an advanced 9% chromium steel. Acta Mater. 49 (2001) 2123-2128.
[14] ASTM Standard E139-11, Standard Test Methods for Conducting Creep, Creep-Rupture, and Stress-Rupture Tests of Metallic Materials, ASTM international, West Conshohocken, PA, 2011.
[15] C.M. Parish, MT3FT-15OR0204122: Report on the acquisition and installation of FEI Talos F200X S/TEM, Oak Ridge National Laboratory (ORNL), Oak Ridge, TN (United States), 2015. http://www.osti.gov/servlets/purl/1234344/.
[16] O. Kwon, J. DeArod, Interactions between recrystallization and precipitation in hot-deformed microalloyed steels. Acta Metall. Mater. 39 (1991) 529-538..
[17] E. Cerri, E. Evangelista, S. Spigarelli, P. Bianchi, Evolution of microstructure in a modified 9Cr--1Mo steel during short term creep. Mater. Sci. Eng., A 245 (1998) 285-292.

[18] M. A. Meyers, K. K. Chawla, Mechanical behavior of materials, Cambridge University Press Cambridge, 2009.
[19] J. S. Lee, H. G. Armaki, K. Maruyama, T. Muraki, H. Asahi, Causes of breakdown of creep strength in 9Cr-1.8W-0.5Mo-VNb steel. Materials Science and Engineering: A 428 (2006) 270-275.
[20] J.H. Kim, T.S. Byun, D.T. Hoelzer, C.H. Park, J.T. Yeom, J.K. Hong, Temperature dependence of strengthening mechanisms in the nanostructured ferritic alloy 14YWT: Part II-Mechanistic models and predictions. Mater. Sci. Eng., A 559 (2013) 111-118.
[21] L. Tan, J.T. Busby, Formulating the strength factor α for improved predictability of radiation hardening. J. Nucl. Mater. 465 (2015) 724-730.

Figures and Captions:

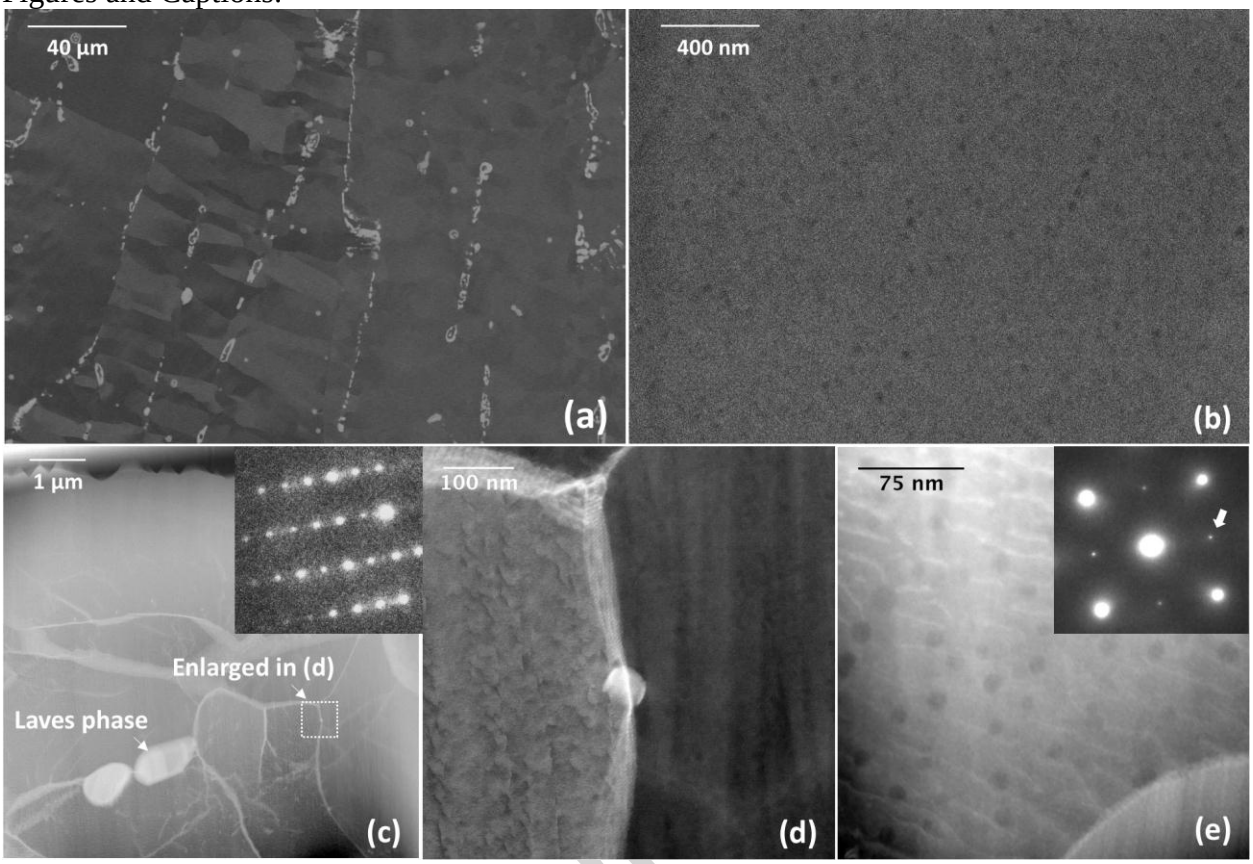

Figure 1. SEM-BSE micrographs of the as-received samples at two magnifications showing (a) grain structure with coarse Laves phase precipitates and (b) B2-type NiAl precipitates. STEM-HAADF micrographs with SAED pattern insets illustrating the morphologies and crystal structures of the (c, d) Laves phase precipitates and (e) B2-type precipitates; (d) is enlarged from the labeled square in (c).

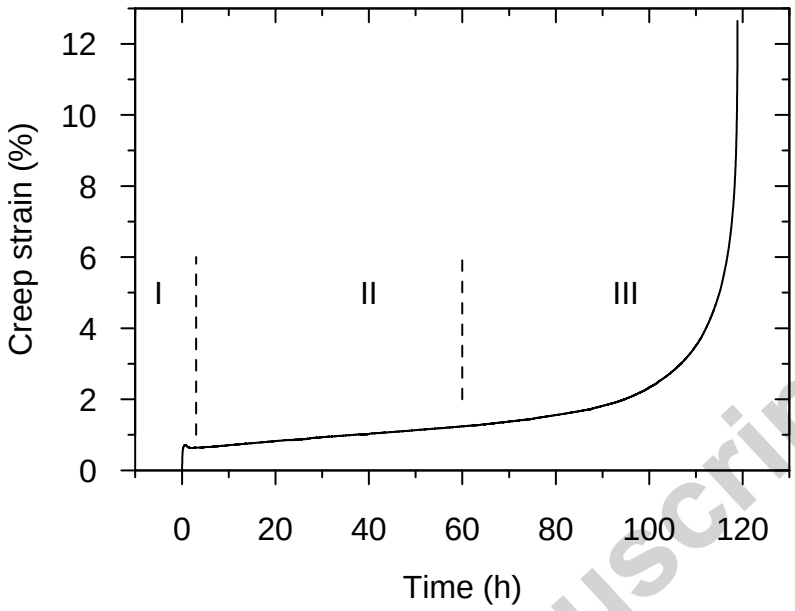

Figure 2. Creep strain-time curve for the test at 650ºC and 120 MPa.

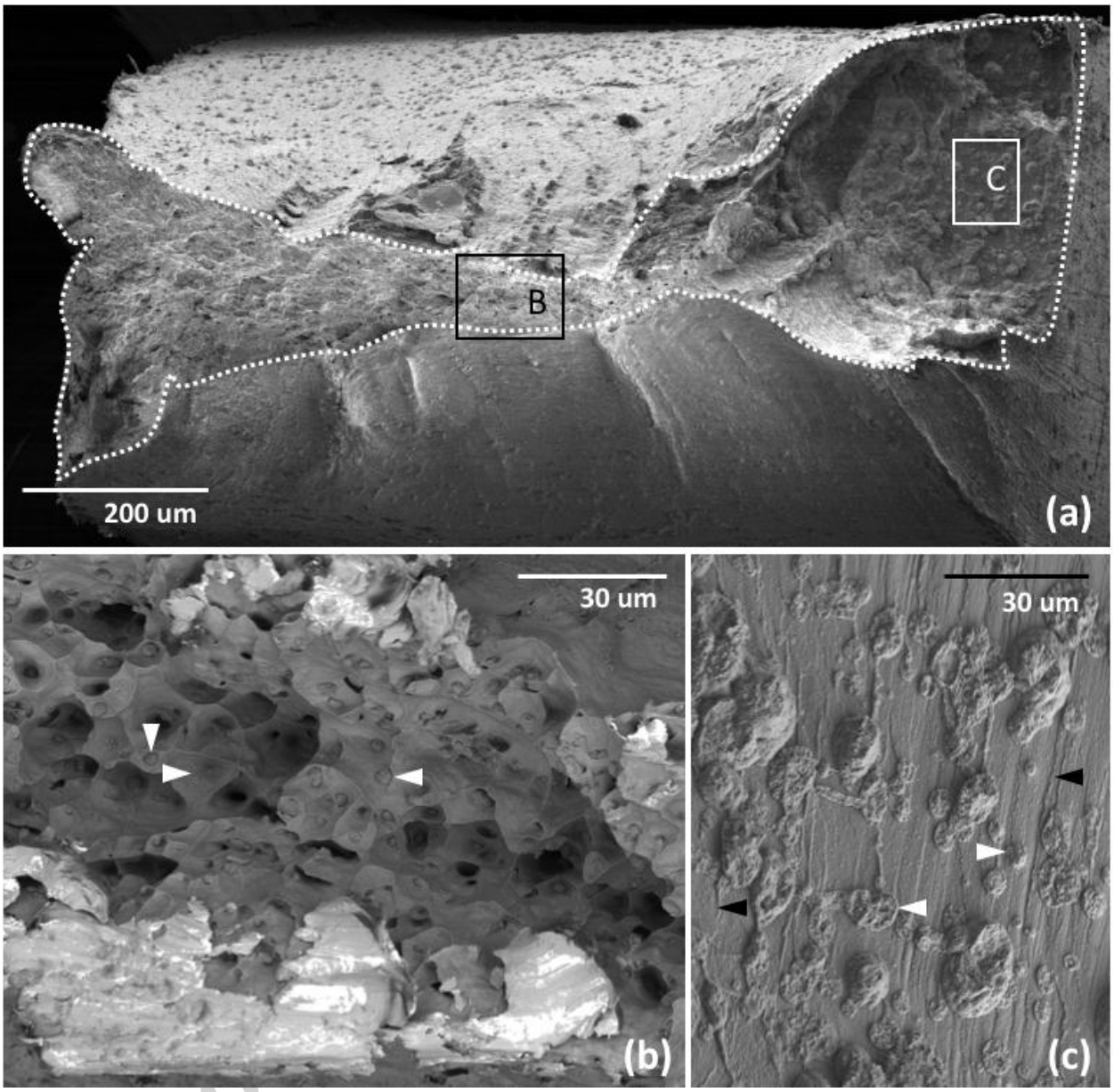

Figure 3. Overview of the (a) creep fracture surface and high magnification micrographs of the (b) ductile and (c) brittle regions. The black boxes in (a) marked as B and C indicate the regions of (b) and (c), respectively. White arrows indicate the Laves phase precipitates, and the black arrows indicate the river marks.

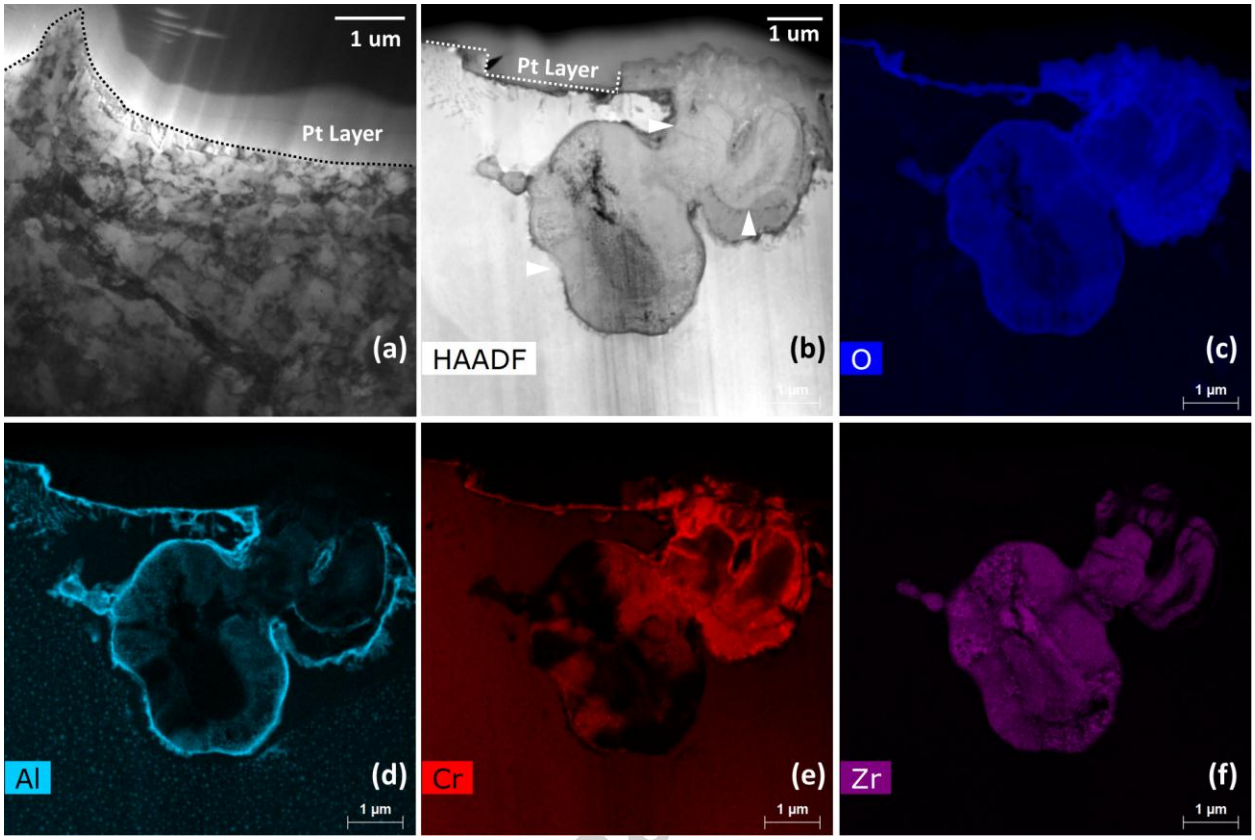

Figure 4. STEM micrographs showing the regions near the (a) ductile (bright-field) and (b) brittle (HAADF) fracture surfaces. (c-f) compositional maps of the brittle sample. The maps were smoothed with a 3×3 pixel smoothing kernel.

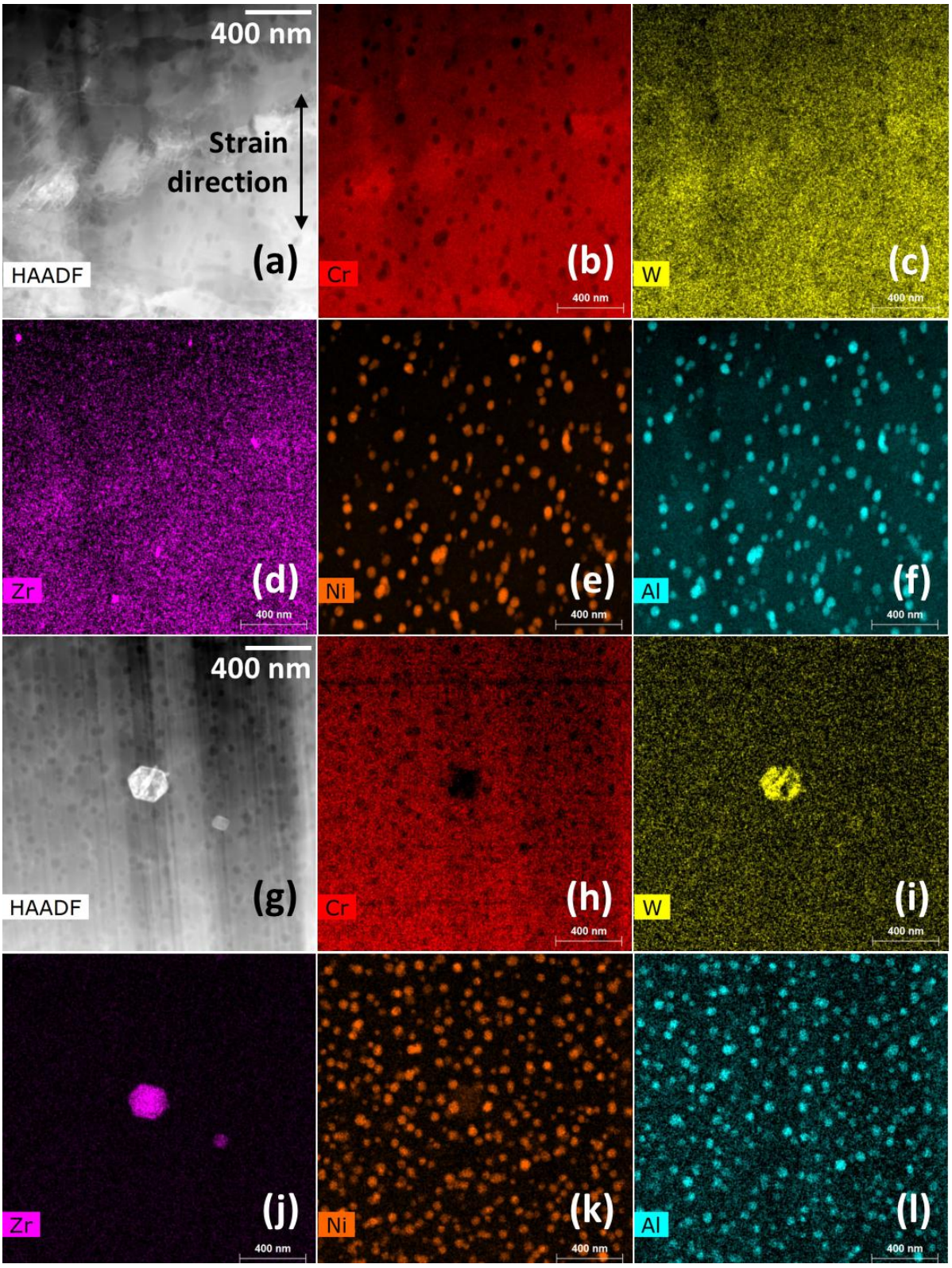

Figure 5. HAADF images and compositional maps of the samples near the ductile fracture in (a-f) and the brittle fracture in (g-l). The applied stress direction is vertical in the images. The maps were smoothed with a 3×3 pixel smoothing kernel.

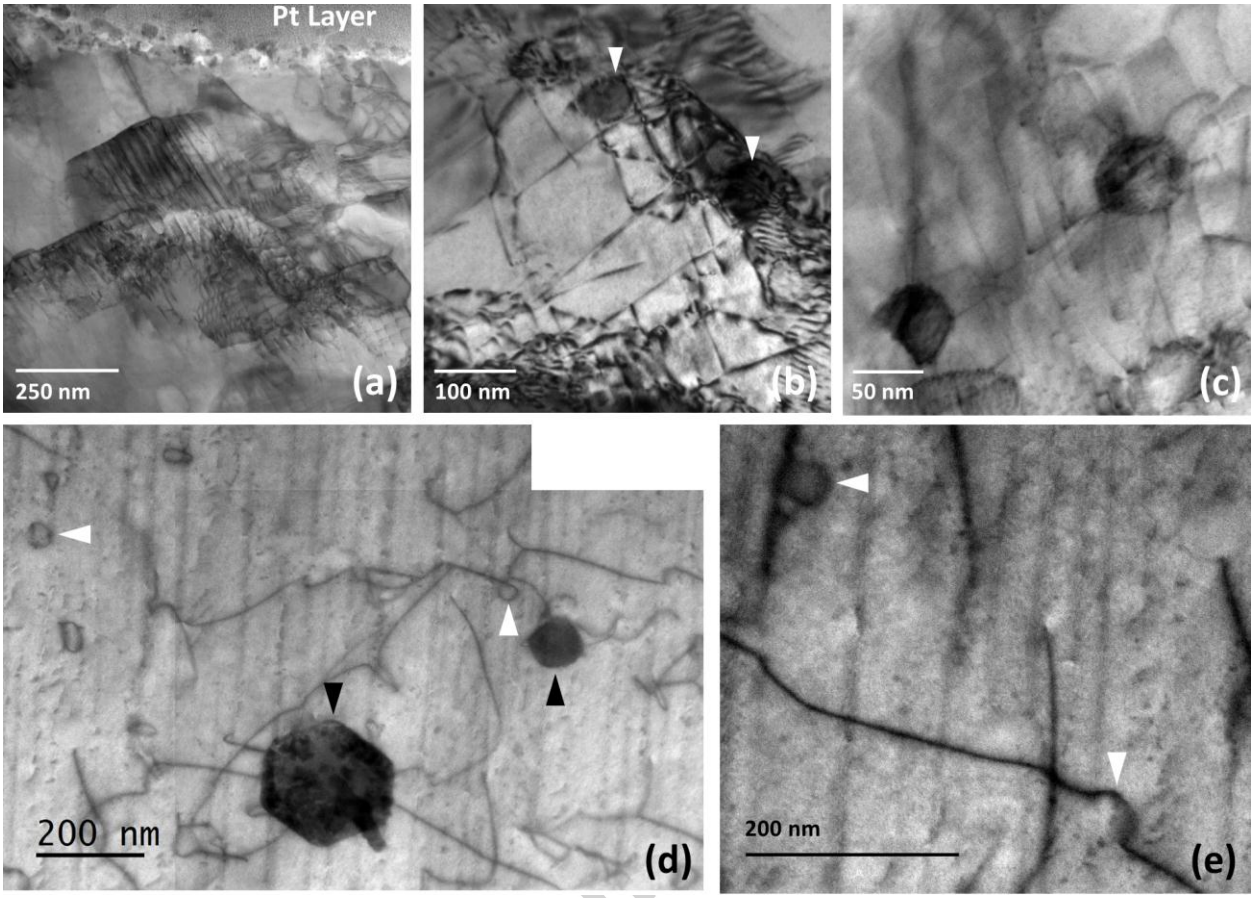

Figure 6. STEM bright-field micrographs: near the ductile fracture surface showing (a) dislocation slip traces and (b-c) coarsened B2 precipitates pinning subgrain boundaries and dislocations; (d-e) near the brittle fracture surface showing the interactions between dislocations and B2/Laves phases.

Tables:

Table 1. Literature reporting precipitation strengthening of different ferritic alloys.

Precipitation phase	Strengthening mechanisms.	Ref.
Coherent B2 NiAl	Orowan bypass and detachment mechanisms.	[5]
Coherent B2 Ni(Al,Fe)	Backstress induced by chemical ordering effect due to minimal lattice misfit and ultra-small precipitate size (< 3 nm).	[6]
Coherent Fe_3Zr	Dislocation-particle interaction.	[7]
Laves	Dislocation and boundary pinning.	[8]
Carbide	Ashby-Orowan mechanism.	[11]

Table 2. Laves and B2 precipitates characterized at the ductile and brittle fracture locations of the creep tested sample.

Precipitates		Fracture type (Area reduction [1])	
		Ductile (~ 80 %)	Brittle (~ 30 %)
Laves phase	Mean diameter (μm) at the fracture surface under SEM [2]	1.7 ± 0.8	6 ± 5
	Mean diameter (nm) beneath the fracture surface.	≤ 40 (Zr-rich precipitates nucleated during the creep test), in addition to ~100 (pre-existing, as seen in the as-received condition)	~50 to ~1000 (pre-existing, with size, morphology and density comparable to the as-received condition)
B2 phase	Mean diameter (nm)	a = 70 ± 20; b = 50 ± 10	a = 50 ± 10
	Number density ($\times 10^{20}$ m^{-3})	1.9 ± 0.6	2.3 ± 0.5
	Volume fraction (%)	1.6 ± 0.8	1.7 ± 0.6
	Morphology	Elongated along the tensile direction	Spherical

[1] Estimated from Fig. 3a referring to the initial dimension of the sample gauge section.
[2] The fracture surface suffered oxidation, tending to cause overestimation for the precipitate sizes